Aerodynamic Design Criteria for Fast Response Probes

H.J. Humm, J.I. Verdegaal
ETH Zürich, Switzerland

1 Introduction

Due to the complexity of aerodynamic fast response probes very often the feasibility of their manufacturing dictates the probes' shape. Additionally, their application in turbomachines imposes some constraints regarding the optimum probe geometry. It was found that prismatic probe bodies fulfil these requirements for fabrication best, furthermore, they are suited for introducing them through very narrow holes in the casing of turbomachines. Also, and above all, the minimisation of the probe size is of the utmost importance.

From the aerodynamic point of view the aspects for fast response probe designs can be divided into static and dynamic criteria:

The desired features of aerodynamic probes based on static design criteria can be summarised as follows: *great calibration range* and *high sensitivity* of the probe and *calibration unaffected by Mach number* (chapter 2).

When introducing aerodynamic probes for dynamic measurements in turbomachines these devices face highly fluctuating flow vectors (in magnitude and direction). Usually, however, aerodynamic probes are calibrated in static flows (e.g. in a wind channel). Applying these static calibration data for interpretations of dynamic flows may result in errors which can considerably deteriorate the quality of the measurement. The aim of this work is to quantitatively determine errors in flow-angle measurement associated with the differences between static and dynamic calibration characteristics (chapter 3). The interpretation of dynamic effects (chapter 4) of the flow around probes leads to their modelling (chapter 5).

2 Static Calibration of Probes

Among the multitude of design criteria for aerodynamic probes, especially for the use in fast response measurements some restrictive demands seem to be important in order to improve the accuracy of the measurement technique.

From a series of prismatic probes (fig. 2-1) calibration data were recorded in a closed-walled wind tunnel ($0.3 < Ma < 1.2$). The geometries varied were **a)** *total apex angle* of the wedge probes from 45 to 90° (probes no. 1, 5 and 6); **b)** relative *locations of the sensing holes* l/c = 0.5 and 0.75 (probe no. 1 & 2), **c)** *nose radius* of the probes r/c = 0 to 20% (probe no. 1, 3 & 4) and **d)** *circular cylinder* (probe no. 7).

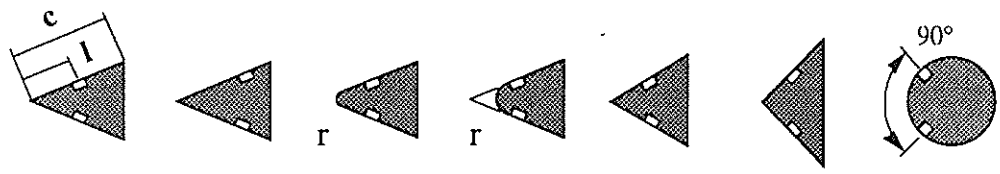

1	2	3	4	5	6	7
wedge 45° l/c = 0.50	wedge 45° l/c = 0.75	wedge 45° l/c = 0.50 r/c = **10%**	wedge 45° l/c = 0.50 r/c = **20%**	wedge 60° l/c = 0.50	wedge 90° l/c = 0.50	circular cylinder

Figure 2-1 *Probes tested in air flow from 0.2 < Ma < 1.2*

The evaluation of the data was performed with emphasis to the following features:

• *Calibration range:* The total calibration range must be greater than the maximum angle of attack (static *and* dynamic, see e.g. GOSSWEILER 1992) encountered during actual measurements in turbomachines. Within the quasi linear calibration range (figure 2-2 part A) not only the description of the calibration data with polynomials is more accurate (see KUPFERSCHMIED 1992) but also sensitivity and indication of static pressure of the probes are almost independent of the angle of attack. However, it is the extension of the unambiguous calibration range which is of primary interest (figure 2-2 part B). The definition for the yaw-angle coefficient K_{12} used in figure 2-2 parts A and B is given by the equation

$$K_{12} = \frac{p_1 - p_2}{p^0 - \frac{p_1 + p_2}{2}}$$

where p_1 and p_2 represent the pressures recorded on the probe according to figure 2-2, p^0 the total pressure of the test flow and $(p_1 + p_2) / 2$ = quasi static pressure indicated by the probe.

Increasing the apex angle of wedge probes leads to greater calibration ranges (probes 1, 5 and 6). A considerable improvement is achieved when placing the sensing hole to the rear of the probe (no. 2: l/c=0.75) or rounded shaping of the leading edge (probes 3 and 4).

• *Yaw sensitivity S* is expressed as the change of pressure difference $p_1 - p_2$ of the probe per degree of yaw in terms of kinetic pressure of the free stream

$$S = \frac{d\, cp_{12}}{d\, \alpha} \qquad cp_{12} = \frac{p_1 - p_2}{\frac{\rho\, u_\infty^2}{2}}$$

A high sensitivity improves the angular resolution of the measurement. Generally, wedge probes with small apex angles exhibit a higher sensitivity. Noteworthy are the findings that a probe with a nose radius of 20% of its chord-length (no. 4 in Fig. 2.2, part C) exceeds the sensitivity of all other configurations tested.

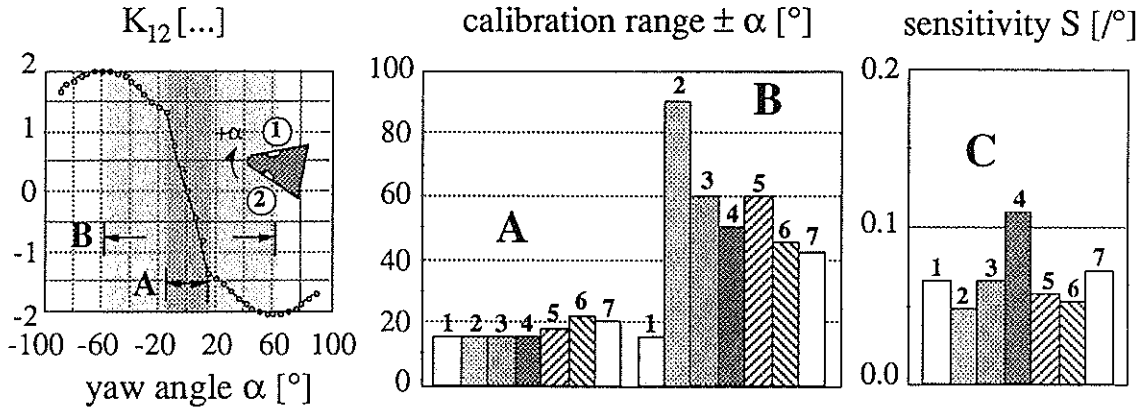

Figure 2-2 *Calibration range [°] (**A**: quasi-linear; **B**: unambiguous) and **C**: sensitivity S = $dcp_{12}/d\alpha$ for the probes tested (Ma = 0.5)*

• The *Mach number influence* on static pressure measurement and sensitivity is shown fig. 2-3 for zero angle of attack ($\alpha = 0°$). A value close to the true free stream static pressure p_∞, when

$$K_s = \frac{p_1 + p_2}{2\,p_\infty}$$

becomes unity, can be measured by using circular cylinders (no. 7, fig. 2-3 for $0 > Ma > 0.5$) or wedge-type probes with either very small total apex angles or locating the sensor to the rear of the probe l/c = 0.75 (no. 2, fig. 2-3). The influence of Mach number on sensitivity S versus Mach number is shown in figure 2-3 to the right. Ideally, a probe should show a constant value over the whole Mach number range.

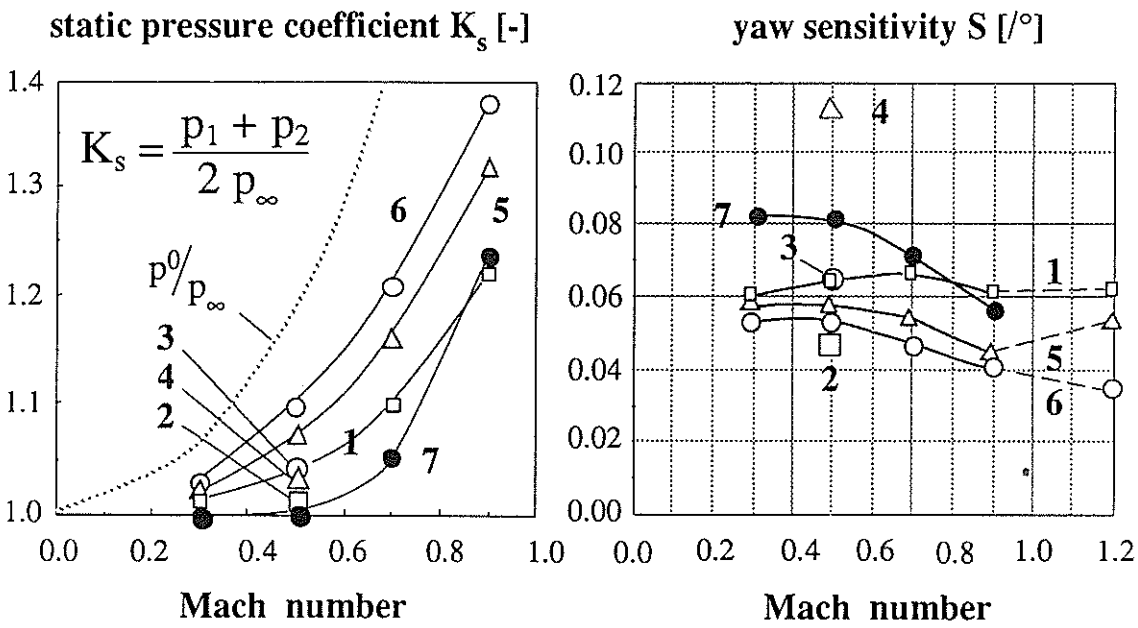

Figure 2-3 *Static pressure coefficient K_s and yaw sensitivity S = $dcp_{12}/d\alpha$ versus Mach number at $\alpha = 0°$*

3 Dynamic Calibration of Probes

The diameters of probes employed for fast response measurements in turbomachines are usually of the order of $1 < d < 6$ mm depending on the number of sensing holes required. With the ground harmonic frequency **f** of the flow fluctuations being identical to the blade-passing frequency in the kHz-domain, free stream velocities u_∞ ranging from 100 to 300 m/s, the governing characteristic non dimensional parameter **k** (reduced frequency) for dynamic flows is of the order

$$k = \frac{f \cdot d}{u_\infty} \approx 0.05 \ldots 0.6$$

with Reynolds numbers

$$Re = \frac{u_\infty d}{\nu} \approx 10'000 \ldots 120'000$$

The experimental simulation of such a dynamic flow environment in air with exactly known conditions lies far beyond the technical possibilities. In the experiments performed at our laboratory sinusoidally oscillating probes were towed relative to the water at rest in a channel of 40 m total length with a cross section of 1 m^2. By using large probes of about 30 mm width in connection with the dynamic viscosity ν of the water the dynamic similarity (reduced frequency, Reynolds number) was followed with very low frequencies of oscillation ($1 < f < 10$ Hz) and low free stream velocities $1 < u_\infty < 5$ m/s.

3.1 Experimental Setup

Figure 3-1 shows the driving mechanism for the angular oscillation of the probes in the water channel and figure 3-2 the geometries of the probes tested.

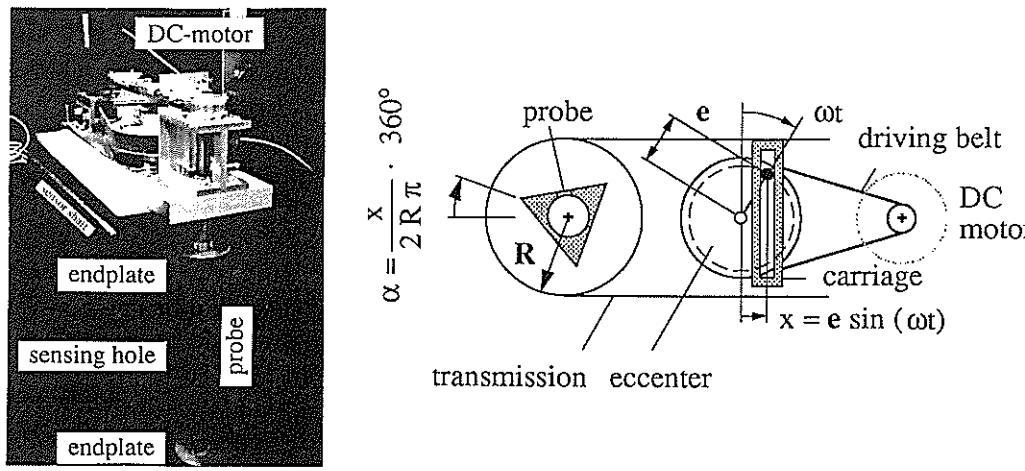

Figure 3-1 Driving mechanism for forced angular probe oscillation

The eccenter, driven by a DC-motor, forces a carriage to perform sinusoidal oscillations in the x-direction. Via a transmission the probe oscillates rotationally around its centre. By varying the eccentricity **e** the amplitude $\hat{\alpha}$ of the angular motion can be determined.

The probes (total length 0.5 m) provided with endplates were cast from epoxy around a stainless steel tube containing the matching part for the sensor shaft. For the 60°-wedge the chordwise location of the sensing hole l/c = 0.25, 0.50 and 0.75 and the relative radius of the leading edge r/c = 0 and 20% was varied. For comparisons, wedge probes with total included angles of 45 and 90° and a circular cylinder were manufactured.

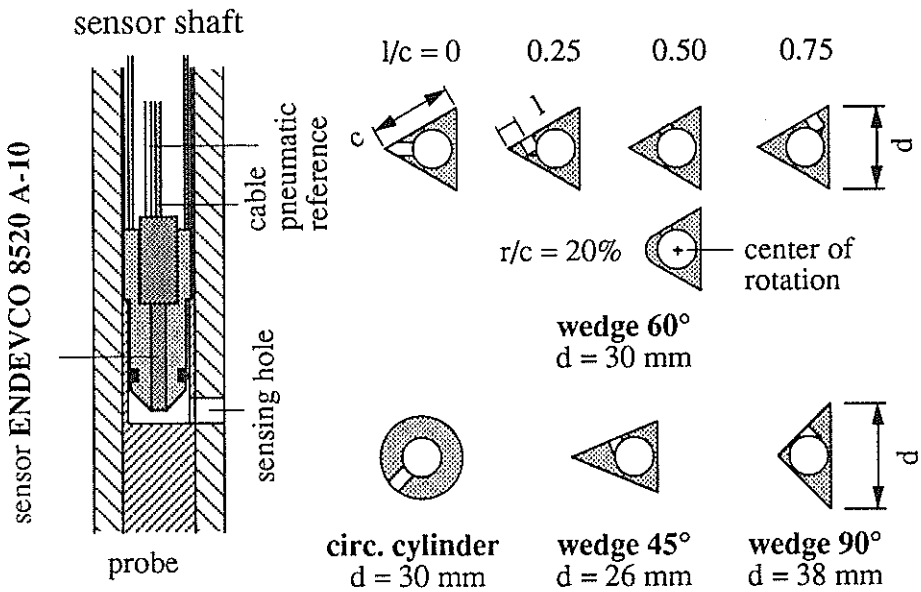

Figure 3-2 Assembly of sensor-shaft and probe geometries tested

3.2 Results

During the experiments the dynamic response of the sensor was instantaneously recorded with the minimum sampling frequency $f_s = 25$ kHz of the data acquisition system. The evaluation of the data was performed in a DEC-Vax environment (HERTER 1992): After digital filtering of the signal (25 Hz) the power spectra were determined in the frequency domain and the ensemble averages formed with respect to a trigger signal. Of this synchronised sampled data the mean dynamic pressure coefficient $\overline{cp_1}$ and standard deviation s were determined and plotted versus the forced angle α of the experiment (fig. 3-3).

$$\overline{cp_1}(\alpha) = \frac{\overline{p_1}(\alpha) - p_\infty}{\frac{\rho u_\infty^2}{2}}\,;\; s(\alpha) = \sqrt{\frac{1}{N-1}\sum_{i=1}^{N}\left(cp_1(\alpha)_i - \overline{cp_1}(\alpha)\right)^2}$$

with $\alpha = \hat{\alpha}\sin(\omega t)$ of the sinusoidal angular motion and $N \approx 50$ representing the number of oscillation cycles. Note that with this procedure for the coefficients $\overline{cp_1}$, in the following denoted as cp_1, all stochastic parts of the signal and frequency components not corresponding to the frequency of oscillation, or higher and subharmonics, are suppressed.

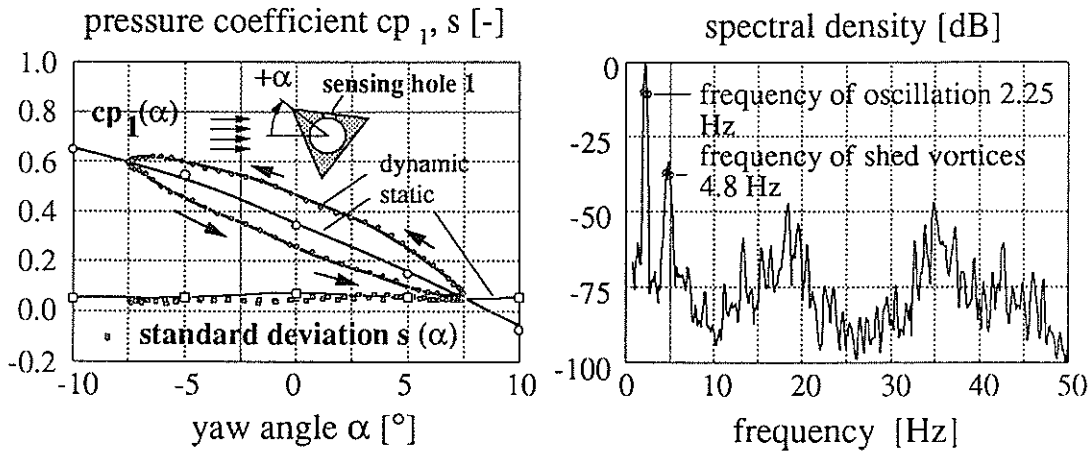

Figure 3-3 *Dynamic pressure coefficient cp_1, standard deviation s and power spectrum for the 60°-wedge probe oscillated with an amplitude of $\hat{\alpha}$ = 7.5° and reduced frequency of k = 0.1; arrows denote the sense of rotation*

The results of the dynamic calibration of the 60°-wedge probe with an amplitude of oscillation of 15° and varied reduced frequency k are presented in fig. 3-4.

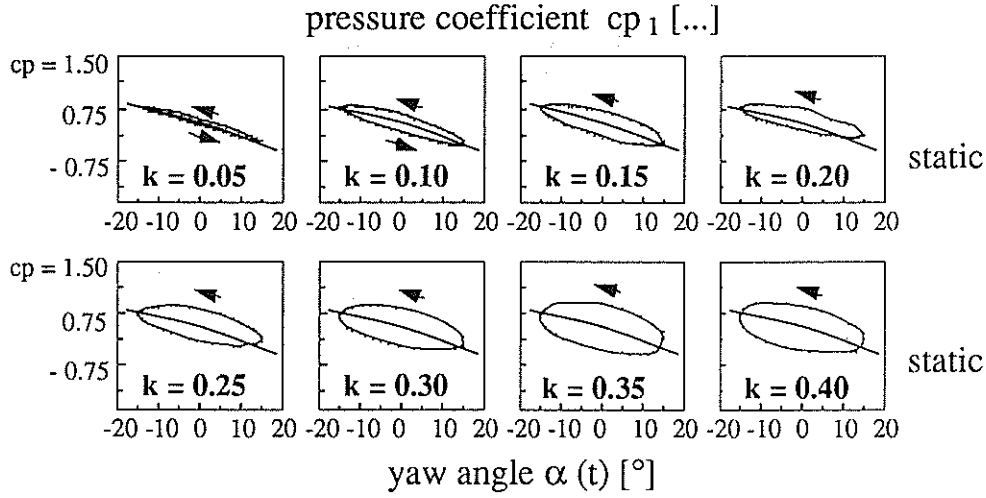

Figure 3-4 *Dynamic calibration data ($\hat{\alpha}$ = 15°) of a wedge probe with a total included angle of 60° in comparison to static values*

With increased frequencies of oscillation the differences between dynamic and static calibration data are seen to become significantly larger.

For technical reasons the probes tested where equipped with one sensing hole only. In order to express the coefficient $cp_{12} = cp_1 - cp_2$ for yaw-angle measurement the opposing value cp_2 was determined from cp_1 by the equation:

$$cp_2(\omega t) = cp_1(\omega t + \pi)$$

presuming the flow pattern in the water-channel to be fully symmetrical.

For the same probe as depicted in figure 3-4 the dynamic calibration data for a constant reduced frequency k = 0.1 but varied amplitude $\hat{\alpha}$ of the oscillation the resulting pressure coefficient cp_{12} is plotted in figure 3-5.

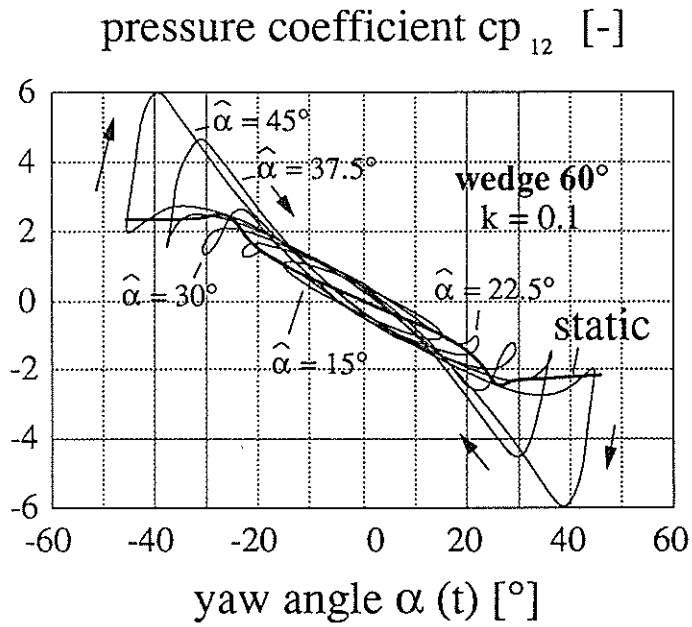

Figure 3-5 *Dynamic calibration data for a 60°-wedge probe, reduced frequency k = 0.1 with different amplitudes of oscillation compared to static curve*

For low amplitudes of oscillation the curves show no hysteresis indicating linear relations between parameters of fluctuation and experiment (see chapter 5). As the amplitude of the oscillation is increased, non-linear effects begin to dominate the calibration data. For the highest amplitude of oscillation tested the dynamic data exceed the static values by approximately a factor of 3. The consequence of these differences between dynamic and static calibration data is that when evaluating the dynamic data applying static calibration we would interpret an angle of attack which does not correspond to the true value (forced yaw angle α of the experiment), as shown in figure 3-6.

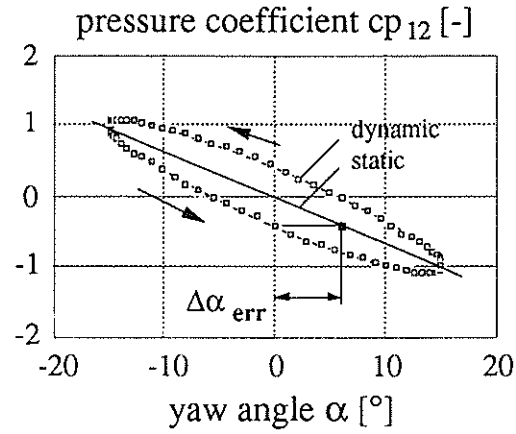

Figure 3-6 *Determination of dynamic error $\Delta\alpha_{err}$*

For a qualitative comparison of the different probe geometries tested (figures 3-7 and 3-8) the dynamic error $\Delta\alpha_{err}$ (deviation between the interpreted and true flow angle) was determined by:

$$\Delta\alpha_{err} = \frac{cp_{12,\,dynamic} - cp_{12,\,static}}{\left.\frac{dcp_{12,\,static}}{d\alpha}\right|_{\alpha=0}}$$

The equation is valid only for the quasi-linear calibration-ranges (where $dcp_{12}/d\alpha$ = const.) but was applied to all configurations leading to an underestimation of the errors in cases where the dynamic values exceed the static calibration range.

The resulting deviations of interpreted flow angle from the true value are shown in figure 3-7 for the 60°-wedge probe and a circular cylinder driven with the same parameters of oscillation.

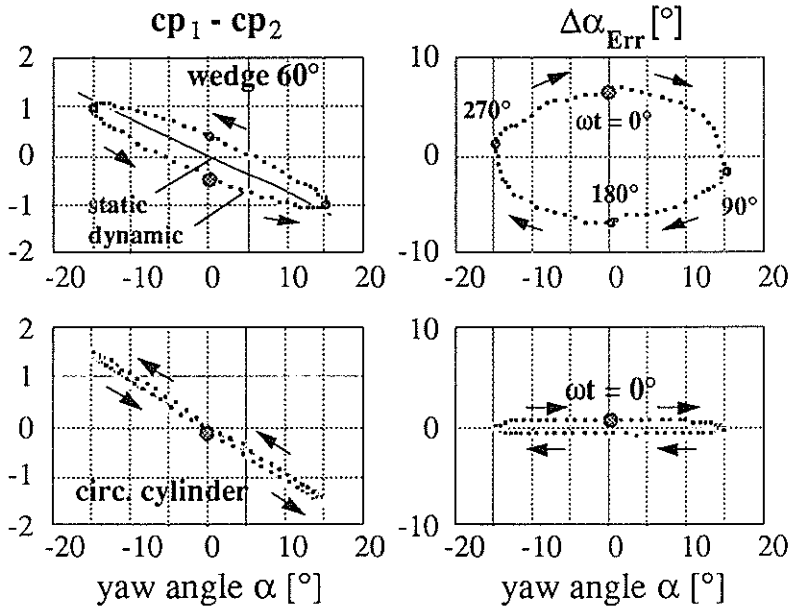

Figure 3-7 *Dynamic calibration data and $\Delta\alpha_{err}$ (misinterpreted flow angle) for a 60°-wedge probe and a circular cylinder oscillated with an amplitude $\hat{\alpha}$ = 15° and a reduced frequency k = 0.1*[1]

Note that e.g. for the wedge probe the maximum misinterpreted flow angle $\Delta\alpha_{err}$ amounts to approximately 50% of the quantity to be measured in a turbomachine which is represented by the amplitude of the forced oscillation $\hat{\alpha}$ = 15° in the experiment.

For a selected group of probe geometries tested the maximum error-angles occurring for varied parameters of oscillation are plotted in figure 3-8.

---

1 The conditions simulated in figure 3-7 would correspond to the measurement of the flow in a turbomachine fluctuating ± 15 ° with a frequency of 6 kHz and a free stream velocity of 250 m/s using a 4 mm probe

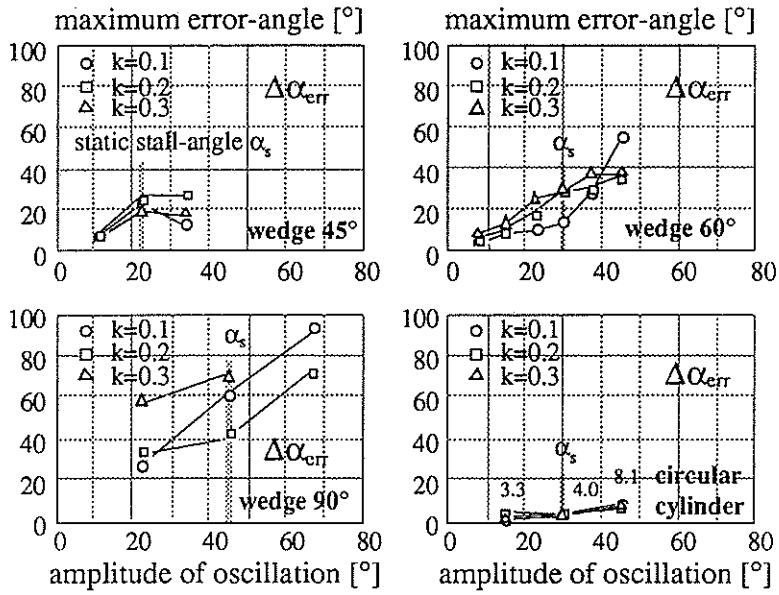

Figure 3-8 *Absolute maximum error-angles for wedge-type probes with total apex angles of 45, 60 and 90° and a circular cylinder as a function of the amplitude of oscillation for three different reduced frequencies k*

To some extent the errors can be seen to depend both on amplitude and frequency of oscillation while the geometry dramatically affects the dynamic errors. For the wedge-type configurations (45 & 60°) in figure 3-8, qualitatively, the errors show an almost linear increase with amplitude of oscillation to approximately the static stall angle (which is of the order of half the apex-angle of the probes). From the probe geometries tested the circular cylinder was least affected by dynamic flow phenomena.

4 Interpretation of dynamic effects

Dynamic flows around bodies comprise a multitude of phenomena of which according to the literature the most important are: *Circulation-induced lift* and *moving wall effects* due to the angular velocity of the relative incidence of the flow vector and *inertia (added mass)* proportional to the angular acceleration. In dynamic flow environments a conceptual different behaviour of unsteady *boundary layers* is observed as well as the phenomenon of *dynamic stall*. Vortex interaction occurs in cases where the frequency of the flow fluctuation is close to the frequency of the naturally shed vortices in the wake of the probe.

Circulation-Induced Lift

A continuously rotating circular cylinder immersed into a uniform free stream generates a lift force proportional the angular velocity. This effect is referred to in the literature as the "Magnus"-effect and can be determined analytically. The general formulation for the local non dimensional pressure cp for any point on the cylinder's surface can be derived from the tangential velocity v_φ at an angle φ relative to the oncoming flow vector when superposing a doublet and a circulation in the potential flow theory.

$$cp = 1 - \frac{v_\varphi^2}{u_\infty^2} = 1 - \frac{4\,u_\infty^2 \sin^2\varphi + 4\,u_\infty\, r\,\dot\varphi \sin\varphi + (r\,\dot\varphi)^2}{u_\infty^2}$$

$$v_\varphi = -\,2\,u_\infty \cdot \sin\varphi - r \cdot \dot\varphi$$

with $2\,u_\infty \sin\varphi$ as the quasi static and $r\,\dot\varphi$ as the "dynamic" term. Assuming a circular cylinder being subjected to a sinusoidal angular oscillation

$$\alpha(t) = \hat\alpha \cdot \sin(\omega t)$$
$$\dot\alpha(t) = \omega \cdot \hat\alpha \cdot \cos(\omega t)$$

the time dependent pressure coefficient cp (t) becomes

$$cp(t) = 1 - \frac{4\,u_\infty^2 \sin^2(\varphi_0 + \alpha(t)) + 4\,u_\infty\, r\,\dot\alpha(t)\,\sin(\varphi_0 + \alpha(t)) + (r\,\dot\alpha(t))^2}{u_\infty^2}$$

for a point under φ_0 from the position of zero angle of attack at $\alpha(t) = 0°$. In figure 4-1 part A the so determined pressure coefficient is plotted versus $\alpha(t)$ at a forward facing point: $\varphi_0 = 0°$ for total pressure and one under an angle of $\varphi_0 = 45°$ or $-45°$, respectively, for yaw angle measurement. Part B shows the theoretically resulting misinterpreted flow angles $\Delta\alpha_{err}$ at $\alpha = 0°$ for the non dimensional description of the angular oscillation

$$\Delta\alpha_{err} = \left.\frac{cp_{12}(t) - cp_{12,\,static}}{\frac{dcp_{12,\,static}}{d\alpha}}\right|_{\alpha=0} = \left.\hat\alpha \cdot \pi \cdot k \cdot \frac{\sin\frac{\pi}{4}}{\sin\frac{\pi}{2}}\right|_{\alpha=0} = \hat\alpha \cdot \pi \cdot k \cdot \frac{1}{\sqrt{2}}$$

according to chapter 3.2 for a circular cylinder with two sensing holes located under $\varphi_0 = \pm 45°$ from the forward facing point.

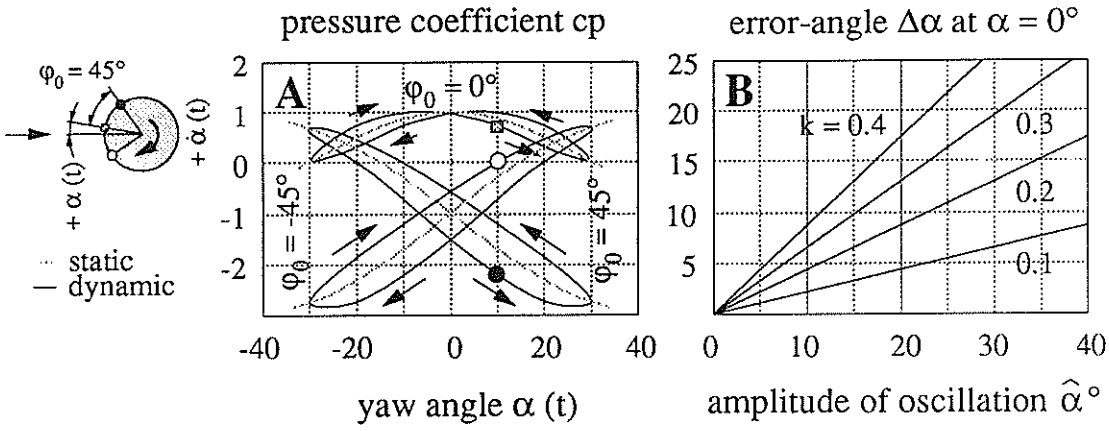

Figure 4-1 *Effect of circulation on pressure on a circular cylinder for non viscous potential flow theory. **A:** pressure coefficient cp for three points on the surface of the cylinder located at $\varphi_0 = 0$ and $\varphi_0 = \pm 45°$ from the stagnation point for the oscillation parameters $\hat\alpha = 30°$ and $k = 0.1$ and **B:** resulting error-angle in yaw-angle measurement for different parameters of oscillation*

The slope and sense of rotation of the dynamic pressure coefficient in part A of figure 4-1 is in good qualitative agreement with the experimental findings, although in the case of the circular cylinder highly overestimated. Note that from the equation of the angular motion it can be derived that the pressure term due to circulation leads the quasi static value by a phase of $\pi/2$. In part B the error-angles $\Delta\alpha_{err}$ are increasing linearly with both frequency and amplitude of oscillation, which is in accordance with the qualitative interpretation of the results in figure 3-8.

Dynamic Boundary-Layers, Moving-Wall Effect

Several authors (e.g. TELIONIS 1981) found that in dynamic flows Prandtl's classical law for boundary layer separation loses its validity. Whilst for static flow conditions the boundary layer will separate when the wall-shear-stress becomes zero, thin layers of reversed flow may exist in dynamic flows without disturbing the "outer flow". Generally, in unsteady flows a delay of flow-separation can be observed (McCROSKEY 1977, NASH/SCRUGGS 1978, etc.). For higher Reynolds numbers the effect of the "moving-wall" plays an important role in the dynamic process influencing the boundary layer transition. Due to the smaller relative velocity between fluid and surface on the downstream moving wall flow transition is delayed whilst on the opposite side it is promoted.

The lift generated by uniformly rotating circular cylinders as a function of the ratio between peripheral and free stream velocity is shown in figure 4-2. The long the boundary layers remain laminar the positive lift for rotating cylinders is maintained (curve **a** in figure 4-2), but severe changes in the generation of lift are observed, when above the subcritical flow regime ($Re > 10^5$) boundary layer transition occurs (ERICSSON 1980).

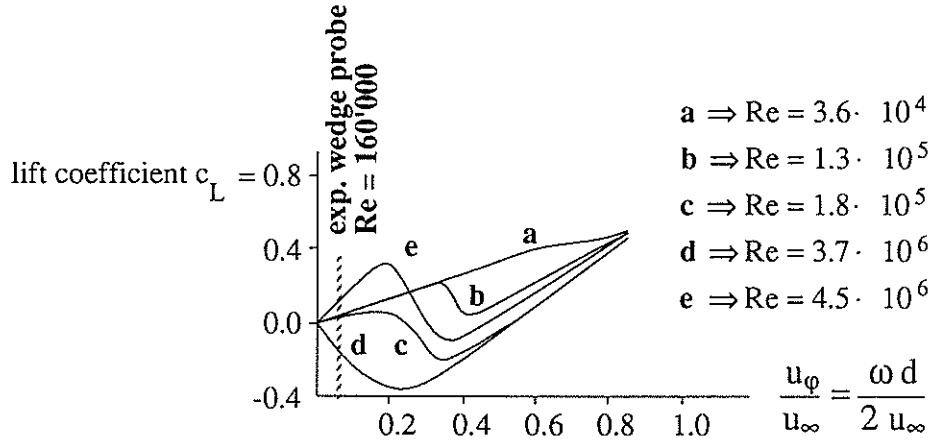

Figure 4-2 *Lift of a uniformly rotating circular cylinder versus peripheral velocity for different flow regimes, adapted from ERICSSON*

These strong effects of the "moving-wall" for circular cylinders are certainly associated with altered conditions for flow separation on the circular cylinder due to earlier or delayed transition. In order to investigate whether the "moving-wall"-effect is also observed when the separation point remains fixed at the trailing edge of probes, experiments were performed for a 60°-wedge type probe in the higher Reynolds number range. To avoid too high free stream velocities and hence too high oscillation frequencies in the experiment a second probe was manufactured by forming a metal sheet around the circular cylinder (figure 4-3).

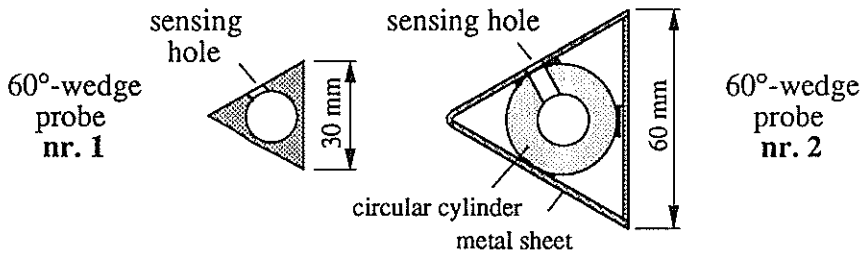

Figure 4-3 *Probe geometries for experiments with higher Reynolds numbers*

In spite of the different probes used in the experiment for Reynolds numbers in the range 20'000 < Re < 80'000 the results show no significant different dynamic calibration data (fig. 4-4). Only by increasing the Reynolds number to Re = 160'000 a distinguishable change in the characteristics is observed (fig. 4-5).

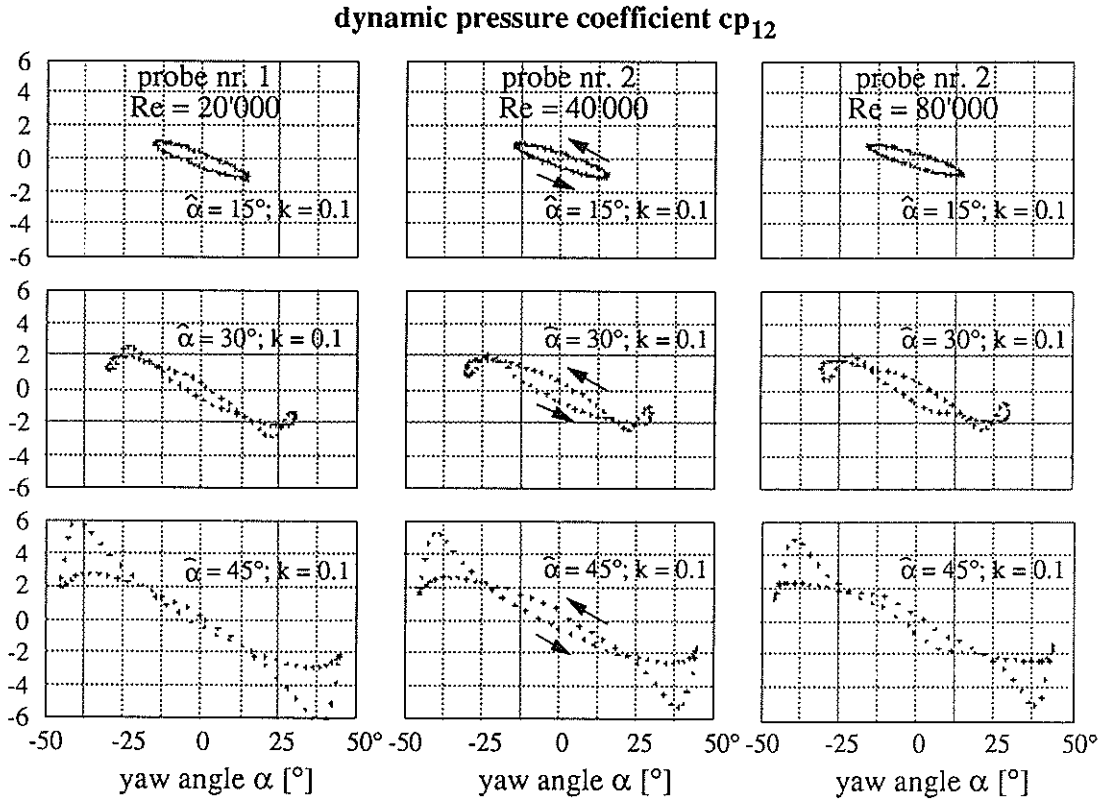

Figure 4-4 *Calibration data for the 60°-wedge type probes for different Reynolds numbers*

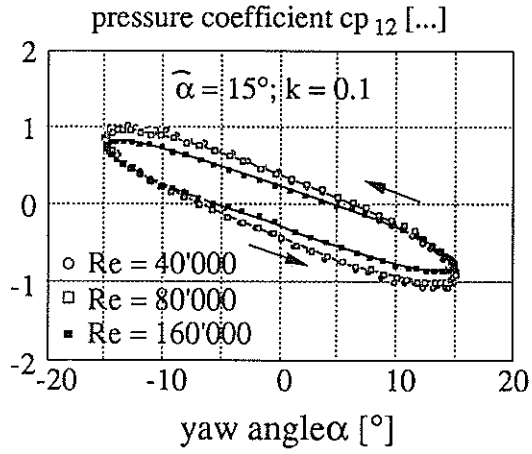

Figure 4-5 *Calibration data for the 60°-wedge type probe no. 2 in the range 40'000 < Re < 160'000*

Inertia (added-mass effects)

The effect of inertia can best be explained by considering a sphere subjected to a flow fluctuating in magnitude, as reported by KOVASZNAY et al. (1981). They found that the local pressure measured on a sphere is the sum of a term proportional to the time variant stagnation pressure $\rho\, c^2/2$ ("quasi static") and a "dynamic" term proportional to the acceleration of the fluid dc/dt

$$p\,(t) = p_\infty + A\,\frac{\rho\, c\,(t)^2}{2} + B\rho a\,\frac{dc}{dt}\,(t)$$

with constants A and B being a function of the peripheral position on the surface. For a sinusoidally fluctuating flow vector (in magnitude) as depicted in figure 4-6, the term proportional to dc/dt always leads the term proportional to $\rho\, c^2/2$ by $\pi/2$.

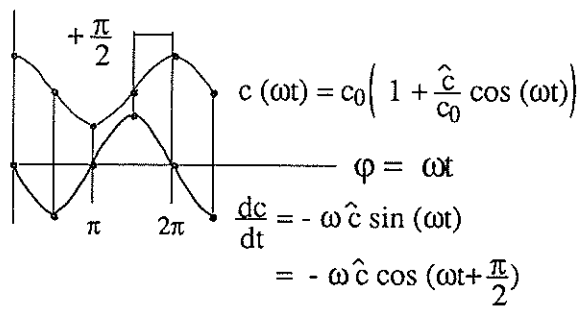

Figure 4-6 *Velocity and acceleration for a sinusoidally fluctuating flow*

By introducing the non dimensional relations for the oscillation the pressure coefficient cp (ωt) which is registered by the probe can be determined as

$$cp\,(\omega t) = \frac{p\,(\omega t) - p_\infty}{\frac{\rho\, c^2\,(\omega t)}{2}} = A \;-\; B\,\frac{2\,\pi\, k\,\frac{\hat{c}}{c_0}\sin\,(\omega t)}{\left(1 + \frac{\hat{c}}{c_0}\cos\,(\omega t)\right)^2}$$

with p_∞ considered to be constant. For the stagnation point of the sphere KOVASZNAY et al. determined by numerical analysis and experiments the coefficients in the equation to be **A = 1.0** and **B = 1.5**.

The coefficient cp (ωt) of the stagnation pressure for different parameters of the fluctuating flow vector is shown in figure 4-7 ($\hat{c}/c_0$ = relative amplitude and k = reduced frequency). Choosing the denominator of the equation above to be the time variant stagnation pressure is, in this case, advantageous since the error in total pressure measurement is directly represented by the difference between the dynamic and quasi static term.

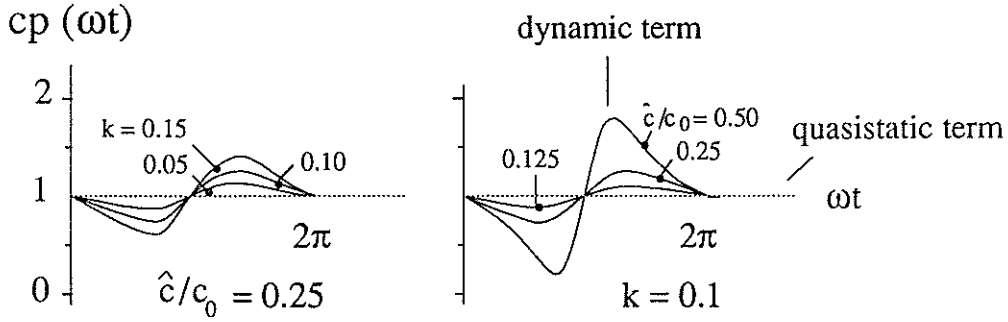

Figure 4-7 *Dynamic pressure coefficient cp for total pressure measurement with a sphere in a fluctuating flow (magnitude)*

For rotational oscillations inertia-effects will occur in an analogue manner, when the fluid is displaced by angular accelerations of the relative incidence of the flow.

Dynamic Stall

According to CARR/McALLISTER/McCROSKEY (1976) the phenomenon of dynamic stall for NACA 0012-profiles occurs due to a separated vortex propagating rearwards from the leading edge, resulting in transient pressure distributions along the surface of the profile promoted by the bursting of a laminar separation bubble (BEDDOES 1980). Classical dynamic stall effects occur only in cases where the static stall angle is exceeded.

The effect of dynamic stall can best be identified by flow visualisation. For the 60°-wedge probe a series of flow patterns is presented in figure 4-8, obtained in a closed-loop continuous flowing water channel. While for ωt = 0° (ωt denoting the angle of the driving mechanism for one period of 360°) the flow on the probe is fully attached, a growing protuberance can be seen at ωt = 50°. At ωt = 90° the vortex has grown larger but is still laminar. From the chordwise pressure distribution, in figure 4-9 plotted over one period of oscillation, the minimum pressure peak at a location l/c = 0.25 can be seen at this time. The minimum pressure at l/c = 0.50 is associated with the downstream propagating vortex at ωt ≈ 130° when the vortex covers almost the whole suction side of the probe. Within a very short time period (125 < ωt < 135°) the centre of the vortex has proceeded from l/c = 0.50 to 0.75 indicated by the minimum pressure peak at l/c = 0.75.

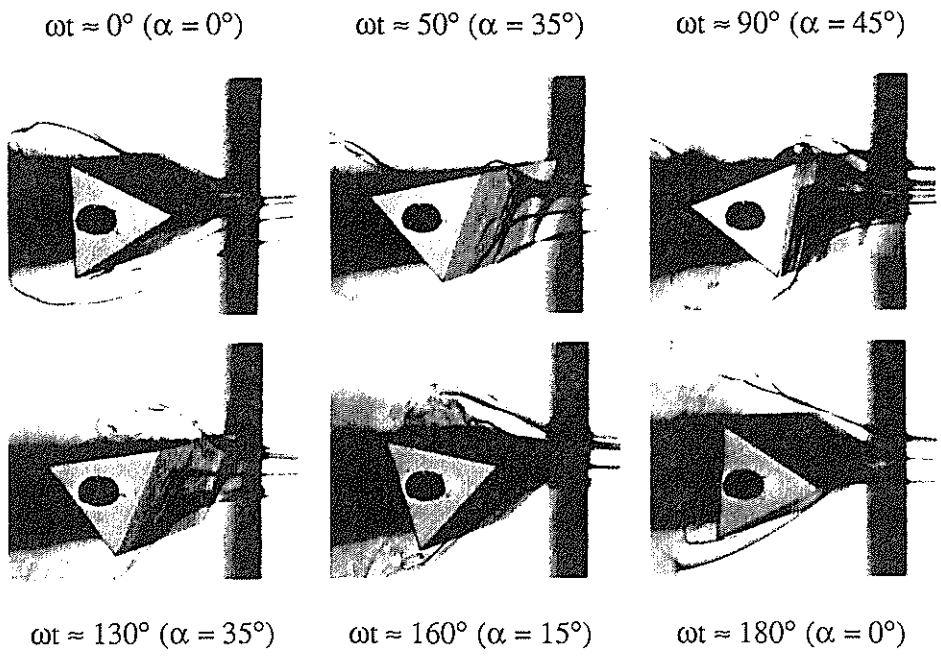

Figure 4-8 *Visualisation of the flow around an oscillating probe (wedge 60°); Re = 5'000; flow from right to left for* $\widehat{\alpha}$ *= 45°, k = 0.1*

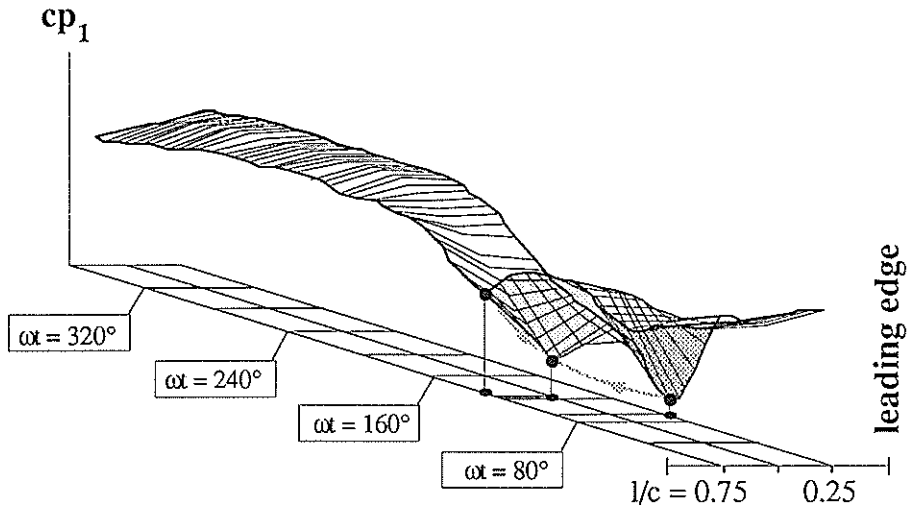

Figure 4-9 *Chord wise non dimensional pressure distribution on the 60°-wedge probe for one loop of oscillation;* $\widehat{\alpha}$ *= 45°, k = 0.1 for three chordwise positions l/c = 0.25, 0.50 and 0.75 (l/c = 0 = leading edge; l/c = 1 = trailing edge)*

Even when facing a very strong pressure gradient (40° < ωt < 160°) in dynamic flow conditions the flow does not separate due to the dynamic response of the boundary- layer described earlier.

The significant difference between static and dynamic ($\widehat{\alpha}$ = 45°, k = 0.1 at ωt = 90°) flow conditions is illustrated in figure 4-10. While for static conditions the flow is fully separated in the dynamic case the flow reattaches behind the laminar separation bubble.

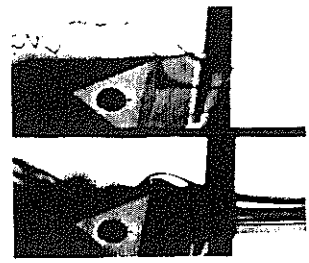

Figure 4-10 *Flow conditions for static (top) and dynamic flow at maximum incidence α = 45°*

From a sequence of video record the extension of the vortex over the suction side of the probe for the same oscillation parameter as in figure 4-8 was determined (figure 4-11: white dots). The shaded areas denote observed transition of the flow in the range $0° < \omega t < 100°$.

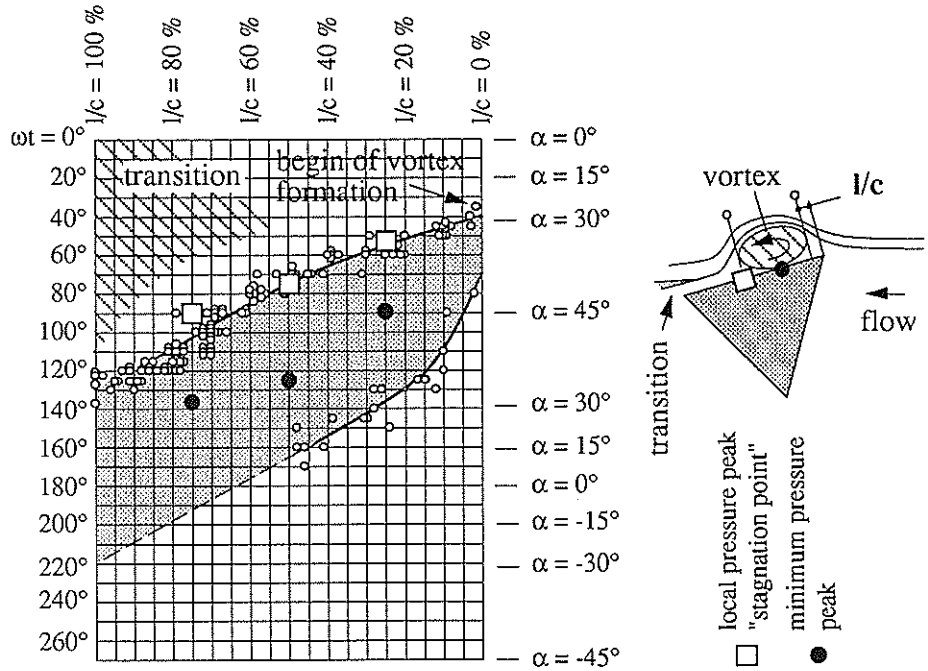

Figure 4-11 *Extension of the vortex over the suction side of the probe (dark shaded area) for the angle of the driving mechanism ωt and corresponding incidence angle α, $\hat{\alpha}$ = 45°, k = 0.1; trailing edge of probe at l/c = 0*

Included into the graph are the independently (towing channel) measured pressures on the probes such as local stagnation points and minimum pressure peaks due to the passing vortex from which the mean velocity of vortex convection $u_c \approx 0.3\ u_\infty$ can be determined.

The occurrence of this severe type of stall is undoubtedly coupled with the formation of a laminar separation bubble at the leading edge when a probe with a sharp leading edge is inclined rapidly beyond its static stall angle. The mechanism of the development of the bubble is due to an influx of fluid from the adjacent stagnation point when the pressure drops on the suction side of the probe.

In order to reduce the dynamic stall effects a wedge probe with the same total included angle (60°) but manufactured with a radius of the leading edge of r/c = 0.2 (c = chord length) was dynamically calibrated (figure 4-12).

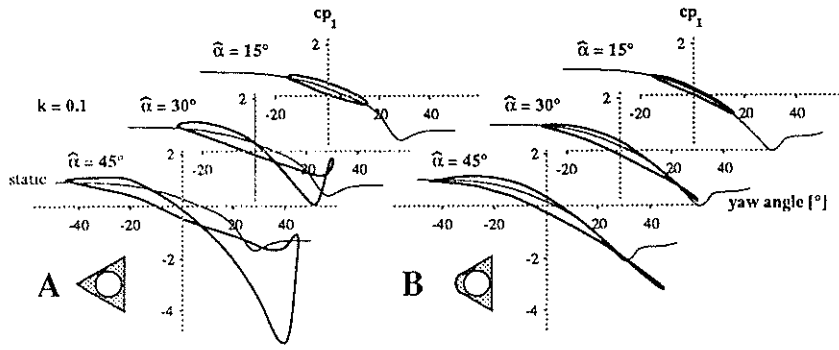

Figure 4-12 Comparison of dynamic calibration data for a 60°-wedge probe with A: sharp leading edge and B: rounded leading edge r/c = 20%

Note that the probe with a radius r/c = 0.2 does not only prove to be almost insensitive to dynamic stall but generally exhibits much better dynamic calibration characteristics.

Interesting were the findings that for a free ending probe (sharp leading edge) the effects of dynamic stall are still present but remarkably reduced compared to the two-dimensional probe (figure 4-13).

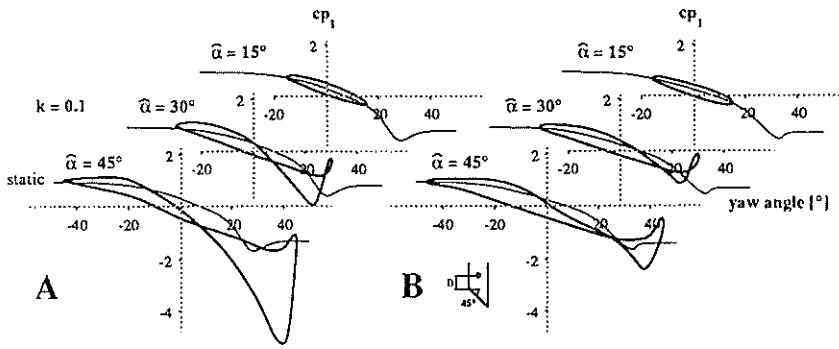

Figure 4-13 Comparison of dynamic calibration data for a 60°-wedge probe: A: two dimensional (aspect ratio L/d ≈ 15, end plate) and B: free ended (d = probe diameter)

Vortex Interaction

Coupling of shed vortices occurs in cases when the frequency of the flow's fluctuation is close to the natural shedding frequency of the vortices. For conditions where the shedding frequency of the vortices in the wake is completely driven by the forced motion of the probe is called "synchronisation". From the power spectra recorded for the configurations tested "synchronisation" was identified (figure 4-14).

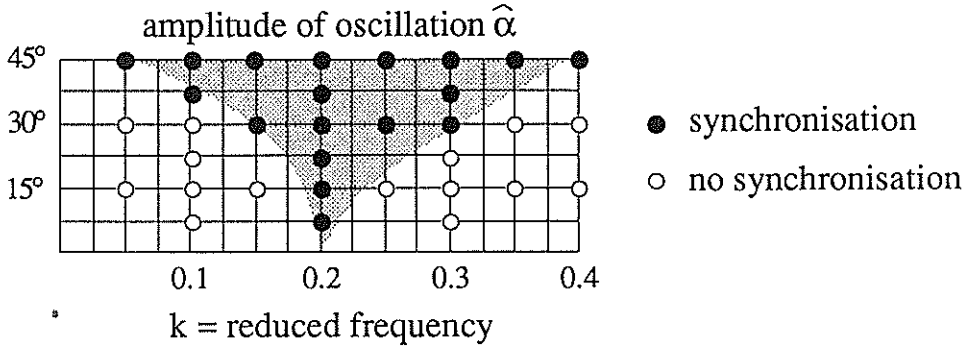

Figure 4-14 *Vortex-synchronisation for the parameters of oscillation (amplitude and reduced frequency) for the 60°-wedge probe (sharp leading edge)*

Although for high amplitudes of oscillation the synchronisation region covers a wide range of frequencies, for all the configurations tested, a tendencial change in the dynamic calibration data was observed only when the frequency of oscillation was very close to the natural shedding frequency of the vortices formed in the wakes of the probes ($0.175 < k < 0.25$). In figure 4-15 the distinctive change of dynamic calibration data when $k = 0.2$ is presented for the example of the oscillating circular cylinder with the resulting error angles, which are significantly higher at $k = 0.2$ compared to $k = 0.1$ and 0.3 respectively.

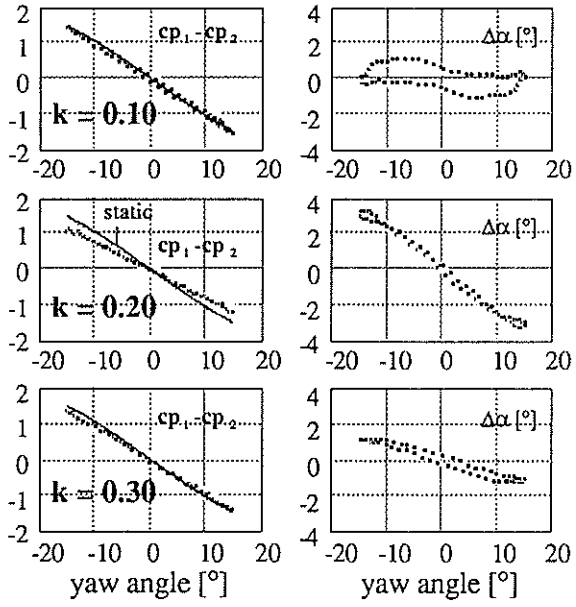

Figure 4-15 *Dynamic calibration of a circular cylinder for three different frequencies of oscillation $0.1 < k < 0.3$ and $\hat{\alpha} = 15°$*

5 Modelling of Dynamic Effects

The modelling of dynamic effects means the description of the dynamic calibration data based on the known true quantities (quasi static) of the flow vector. From the experiments it has been found that within limits the dynamic effects show a systematic increase with amplitude and frequency of oscillation. Qualitatively, from chapter 3.3, different dynamic effects have been identified but the magnitude of their contribution to the dynamic response of the probe in the measurement is unknown. While e.g. circulation will act proportional to the angular velocity of the probes during the experiments, inertia will occur due to angular accelerations of the forced motion. Dynamic stall and vortex interaction have to be considered as the limits of the modelling.

The modelling described in the following is of empirical character. By adding numerical constants to the first (e.g. circulation) and second derivative (e.g. inertia) of the angular motion

$$cp_{12,\,modelled}\ (\omega t) = cp_{12,\,static}\ (\omega t) + C_1 \frac{d\alpha}{dt}\ (\omega t)\ + C_2 \frac{d^2\alpha}{dt^2}\ (\omega t)$$

the dynamic response of the oscillating probe (60°-wedge) can be modelled using a least squares approximation (figure 5-1).

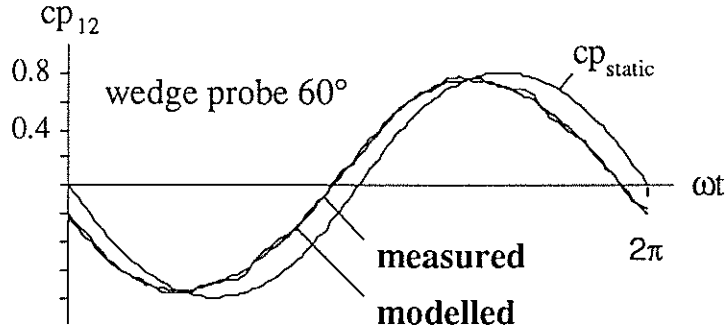

Figure 5-1 Modelling of dynamic effects for the 60°-wedge probe, $\hat{\alpha}$ = 11.25°, k = 0.075

Due to the phase shift of $\pi/2$ between α and $\mathbf{d\alpha/dt}$ and π between α and $\mathbf{d^2\alpha/dt^2}$ in the experiment, the effects due to e.g. circulation and inertia will dominate the dynamic response of the probe to the forced oscillation at different stages of the motion.

At $\alpha = 0°$ during the oscillation the effect of inertia should become 0 since the second derivative of the motion $d^2\alpha/dt^2 = 0$. In this case only differences between dynamic and quasi static calibration data due to circulation should be present, i.e. the resulting error angles would show a linear relation with respect to the amplitude $\hat{\alpha}$ and reduced frequency k of the oscillation. On the other hand, when $\alpha = \hat{\alpha}$ where $d\alpha/dt = 0$, the resulting error-angles due to inertia should become a function of $\hat{\alpha}$ and the squared reduced frequency k.

For a number of oscillation parameters the mean values for the constants $C_{\dot{\alpha}}$ and $C_{\ddot{\alpha}}$ were determined accordingly to the equations given above and the modelled error-angles $\Delta\alpha_{err}$ as a function of $\hat{\alpha}$ and reduced frequency k compared to the experiment (figure 5-2).

$$\Delta\alpha_{err} = C_{\dot{\alpha}} \cdot k \cdot \hat{\alpha}, \text{ at } \alpha = 0 \text{ for } \omega t = 0 \text{ and } 180°$$
$$\Delta\alpha_{err} = C_{\ddot{\alpha}} \cdot k^2 \cdot \hat{\alpha}, \text{ at } \alpha = \pm\hat{\alpha} \text{ for } \omega t = 90 \text{ and } 270°$$

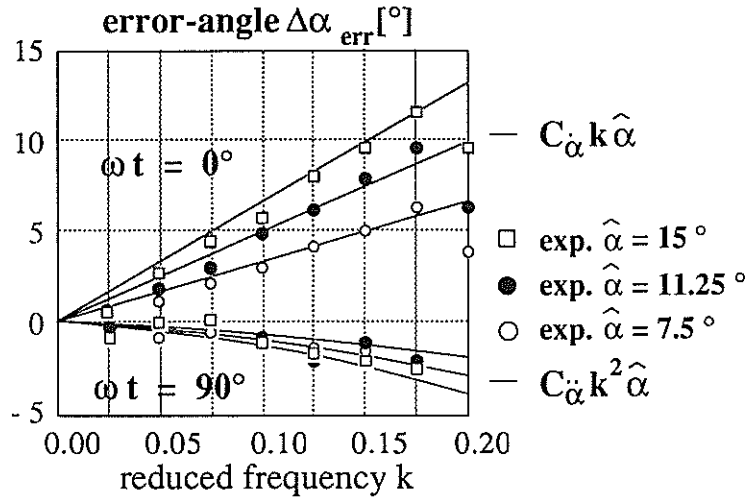

Figure 5-2 Error angles due to dynamic effects at ωt = 0° and 90° for the 60°-wedge probe

The good agreement between the modelled error-angles and the experiments within the range 0 < k < 0.175 substantiates the linear relations between the error-angle and $\hat{\alpha}$ and k at ωt = 0° (α = 0°), although the bending of the curves indicates weak non-linear dynamic effects. Despite the scatter of the experimental data the tendencial agreement between the modelled error-angles and the experiments can be seen clearly at ωt = 90° ($\alpha = \hat{\alpha}$).

6 Conclusions

From the static aerodynamical point of view the ideal probe design will be a compromise between the different aspects shown in chapter 2. For various applications yaw meters indicating the true static pressure of the free stream are desirable, although in most applications, where probes are thoroughly calibrated, a clear relation of K_S as a function of Mach number can be determined. Additionally, advantages like the high sensitivity of sharp wedges are far outweighed by disadvantages associated with errors arising from exceeded calibration ranges during measurements.

In the experiments (dynamic calibration) the fluctuation of the relative incidence angle to the probes was simulated by moving oscillating probes in a fluid at rest, while in turbomachines stationary probes are subjected to a fluctuating flow. Although, according to literature, there is from the kinematical point of view no difference between the two cases the experiment will hardly represent the true flow conditions in every detail. However, one shall assume that the gross flow patterns will be the same when the flow in the turbomachine rapidly changes its angle relative to the probe. The conclusions to be drawn from the experiments are that for given flow conditions in a turbomachine the maximum incidence angle of the relative flow vector must not exceed the dynamic calibration range where modelling of the dynamic effects is feasible - this is achieved by choosing a probe geometry where no dynamic stall occurs which takes place when the static stall angle is exceeded. Furthermore it has been found that the long no vortex interaction (k ≈ 0.2) occurs, the dynamic error is directly to be related to the non dimensional frequency parameter k and thus to the probe size. Even when probe size is fixed, e.g. for technical reasons, still the possibility is given to apply probe geometries which are affected by an order of magnitude less by dynamic effects.

7 Acknowledgements

This work is supported by the Swiss National Science Fund. Additionally, the authors would like to thank Dr. D. Herter for making available the evaluation of the data on the Vax-computer and Mr. P. Lehner for his technical assistance.

8 References

BEDDOES T.S. 1980
A qualitative Discussion of Dynamic Stall
AGARD-R-679 Special Course on Unsteady Aerodynamics

CARR L.W., MCALISTER K.W., MCCROSKEY W.J. 1976
Dynamic Stall Experiments on Oscillating Airfoils
AIAA Journal V14 N1

ERICSSON L.E. 1980
Karman Vortex Shedding and the Effect of Body Motion
AIAA Journal V18 N8

GOSSWEILER C., KUPFERSCHMIED P. 1992
Fast Response Aerodynamic Probe Measurements in a Turbulent Pipe Flow
XIth Symposium on "Measuring Techniques for Transonic and Supersonic Flows in Cascades and Turbomachines", Hochschule der Bundeswehr München, Germany 1992

HERTER D., GOSSWEILER C., CHRISANDER N.O. 1992
AW-System - An Interactive Environment for the Evaluation of Large Time Series
XIth Symposium on "Measuring Techniques for Transonic and Supersonic Flows in Cascades and Turbomachines", Hochschule der Bundeswehr München, Germany 1992

KOVASZNAY L.S.G., TANI I., KAWAMURA M., FUJITA H. 1981
Instantaneous Pressure Distribution Around a Sphere in Unsteady Flow
Journal of Fluids Engineering Vol. 103

KUPFERSCHMIED P., GOSSWEILER C. 1992
Calibration, Modelling and Data Evaluation Procedures on the Example of a Four Hole Probe
XIth Symposium on "Measuring Techniques for Transonic and Supersonic Flows in Cascades and Turbomachines", Hochschule der Bundeswehr München, Germany 1992

MCCROSKEY W.J. 1977
Some Current Research in Unsteady Fluid Dynamics-THE FREEMAN SCHOLAR LECTURE
Journal of Fluids Engineering 1977

NASH J.F., SCRUGGS R.M. 1978
Unsteady Boundary- Layers With Reversal and Separation
AGARD CP 227

STEARNS S.D. 1975
Digital Signal Analysis
Hayden Book Company N.Y., U.S.A.

TELIONIS D.P. 1981
Unsteady Viscous Flow
Springer